Dr.Paul.Kinsler@physics.org
http://www.kinsler.org/physics/

arXiv:physics/0212016v2 [physics.optics] 4 Sep 2003

Few Cycle Pulse Propagation

P. Kinsler and G.H.C. New
Department of Physics, Imperial College, Prince Consort Road, London SW7 2BW, United Kingdom.
(Dated: February 5, 2022)

We present a comprehensive framework for treating the nonlinear interaction of few-cycle pulses using an envelope description that goes beyond the traditional SVEA method. This is applied to a range of simulations that demonstrate how the effect of a $\chi^{(2)}$ nonlinearity differs between the many-cycle and few-cycle cases. Our approach, which includes diffraction, dispersion, multiple fields, and a wide range of nonlinearities, builds upon the work of Brabec and Krausz[1] and Porras[2]. No approximations are made until the final stage when a particular problem is considered.

The original version (v1) of this arXiv paper is close to the published Phys.Rev.A. version, and much smaller in size.

PACS numbers: 42.65.Re,42.65.Yj,42.65.-k,31.15.-p

NOTE: this is a longer version of a paper published as Phys. Rev. A **67***, 023813 (2003). It therefore contains the same text and graphics, but has additional remarks and many extra figures, most notably more complete sets of simulation results. This has led to some repetitions in the text, and also some of the extra figures have artifacts: for example, the envelope phase graphs when the envelope has a small magnitude, and some of the figures showing the phase drift have spikes where a stable value could not be found. Further, some figures pass without much comment.*

I. INTRODUCTION

The analysis of optical pulse propagation traditionally involves describing a pulse in terms of a complex field envelope, while neglecting the underlying rapid oscillations at its carrier frequency. The resulting "slowly varying envelope approximation" (SVEA) (see e.g. [3]), which reduces second order differential equations to first order, is valid when the envelope encompasses many cycles of the optical field and varies slowly. The alternative approach is to solve Maxwell's equations numerically (see e.g. [1, 4]), which is more general but involves greater computational effort, and lacks the intuitive picture of a pulse "envelope".

For example, optical parametric oscillators (OPOs) based on aperiodically-poled lithium niobate (APPLN) have generated 53 fs idler pulses at 3μm that are nearly transform limited, and contain only five optical cycles [5]; laser pulses with less than three optical cycles have been generated in other contexts [6]. Under these circumstances, the validity of the slowly-varying envelope approximation is clearly open to question.

Brabec and Krausz [1] derived corrections to the SVEA, which they included in their "slowly evolving wave approximation" (SEWA). This enabled the few-cycle regime to be modelled with improved accuracy, and the SEWA has subsequently been applied in different situations, including ultrashort IR laser pulses in fused silica [7, 8], the filamentation of ultra-short laser pulses in air [9], and even in microstructured optical fibres [10]. Later, Porras [2] proposed a slightly different "slowly evolving envelope approximation" (SEEA) that included corrections for the transverse behavior of the field.

Here we use a field envelope approach to simulate the propagation of ultrashort pulses in a $\chi^{(2)}$medium. The novelty is that we (a) derive a more general form than that of Brabec and Krausz, called the "generalised few-cycle envelope approximation"(GFEA); and (b) apply it to both optical (non-degenerate) parametric amplification (NPA), and the optical parametric oscillator (OPO). A shorter version of this paper has been published in Phys. Rev. A [11]. The only previous multiple field application of this kind of result was for four wave mixing [12].

We compare the SEWA/SEEA equations to our own (section II), and explain the differences and subsequent adjustments to the necessary approximations. This theory enables us to rigorously study what combination of approximations affords the most efficient method for treating a given nonlinear interaction involving few-cycle pulses. Next (section III) we discuss the $\chi^{(2)}$ nonlinearity and a scaling scheme designed to reveal the few-cycle effects. Then we compare the SVEA predictions to the few cycle GFEA theory using idealised situations (section IV) and more realistic OPO models (section V). Finally, we present our conclusions (section VI).

II. THEORY

This section contains a summary of a complete rederivation [13] of a Brabec & Krausz style theory, which yields an evolution equation for an envelope description of pulse propagation in the few-cycle regime. Our result is more complicated than the SEWA equation [1], but reduces to it in the appropriate limits; it also explains the slight differences between their result and that of Porras [2].

Following Brabec-Krausz, we consider the case of small transverse inhomogeneities of the polarization, and so start with the three dimensional wave equation

$$\left(\partial_z^2+\nabla_\perp^2\right)E(\vec{r},t)-\frac{1}{c^2}\partial_t^2\int_{-\infty}^{t}dt'\varepsilon(t-t')E(\vec{r},t') = \frac{4\pi}{c^2}\partial_t^2 P_{nl}(\vec{r},t). \quad (1)$$

Here $\nabla_\perp^2$ is the transverse Laplace operator, ∂_α is shorthand notation for $\partial/\partial\alpha$, $\varepsilon(t) = (2\pi)^{-1}\int_{-\infty}^{\infty} d\omega\tilde{\varepsilon}(\omega)e^{\imath\omega t}$, $\tilde{\varepsilon}(\omega) = 1 + 4\pi\chi(\omega)$, and $\chi(\omega)$ is the linear electric susceptibility. The electric field E propagates along the z direction. Both E and the nonlinear polarization P_{nl} are polarized parallel to the x axis.

We can transform eqn. (1) into frequency space in order to expand $\tilde{\varepsilon}(\omega)$ in powers of ω, thus enabling us to treat the material parameters as a power series which we can truncate to an approriate order. However for simplicity it is better to expand k about a suitable ω_0 instead. Using $\tilde{\varepsilon}(\omega) = c^2k(\omega)^2/\omega^2$, it follows that

$$\begin{aligned} k(\omega) &= \sum_{n=0}^{\infty} \frac{\gamma_n(\omega-\omega_0)^n}{n!}; \\ \gamma_n &= \partial_\omega^n k(\omega)|_{\omega_0} = \beta_n + \imath\alpha_n; \beta_n, \alpha_n \in \mathbb{R}. \end{aligned} \tag{2}$$

We can now write the frequency space version of eqn. (1) as

$$\begin{aligned} &\left(\partial_z^2 + \nabla_\perp^2\right) E(\vec{r},t) + \left[\sum_{n=0}^{\infty} \frac{\imath^n\gamma_n(\partial_t + \imath\omega_0)^n}{n!}\right]^2 E(\vec{r},t) \\ &= \frac{4\pi}{c^2}\partial_t^2 P_{nl}(\vec{r},t). \end{aligned} \tag{3}$$

We introduce an envelope and carrier form for the field in the usual way, using $\vec{r} \equiv (\vec{r}_\perp, z)$, so that

$$E(\vec{r},t) = \quad A(\vec{r}_\perp,z,t)e^{\imath\Xi} + A^*(\vec{r}_\perp,z,t)e^{-\imath\Xi}, \tag{4}$$

and similarly $P_{nl}(\vec{r},t) = B(\vec{r}_\perp,z,t;A)e^{\imath\Xi} + B^*(\vec{r}_\perp,z,t;A)e^{-\imath\Xi}$. The symbol $\Xi = \beta_0 z - \omega_0 t + \psi_0$ is introduced as a convenient shorthand for the argument of the exponential. With these envelope-carrier substitutions, the equation of motion can be written as

$$\begin{aligned} &\left([\imath\beta_0 + \partial_z]^2 + \nabla_\perp^2\right) A(\vec{r}_\perp,z,t) \\ &+ \left[\sum_{n=0}^{\infty} \frac{\gamma_n\omega_0^n}{n!}\left(\frac{\imath}{\omega_0}\partial_t\right)^n\right]^2 A(\vec{r}_\perp,z,t) \\ &= -\frac{4\pi\omega_0^2}{c^2}\left(1 + \frac{\imath}{\omega_0}\partial_t\right)^2 B(\vec{r}_\perp,z,t;A). \end{aligned} \tag{5}$$

Eqn. (5) has the opposite sign on the RHS to Brabec & Krausz's eqn. (2), but agreement is recovered later in eqn. (11).

As is usual, we introduce co-moving variables

$$\tau = \omega_0(t - \beta_1 z), \quad \partial_t \equiv \omega_0\partial_\tau, \tag{6}$$

$$\xi = \beta_0 z, \quad \partial_z \equiv \beta_0\partial_\xi - \omega_0\beta_1\partial_\tau, \tag{7}$$

and eqn. (5) now becomes

$$\begin{aligned} &\left\{\left(\imath\beta_0 + \beta_0\partial_\xi - \omega_0\beta_1\partial_\tau\right)^2 + \nabla_\perp^2 + \left[\sum_{n=0}^{\infty}\frac{\gamma_n\omega_0^n}{n!}(\imath\partial_\tau)^n\right]^2\right\} \\ &\times A(\vec{r}_\perp,\xi,\tau) + \frac{4\pi\omega_0^2}{c^2}(1+\imath\partial_\tau)^2 B(\vec{r}_\perp,\xi,\tau;A) = 0. \end{aligned} \tag{8}$$

For convenience we also introduce the dimensionless ratio of phase and group velocities $\sigma = \omega_0\beta_1/\beta_0 = (\omega_0/\beta_0)/(1/\beta_1) = v_f/v_g$, and use the fact that the refractive index at ω_0 is $n_0 = c\beta_0/\omega_0$. We also define a dispersion term $\hat{D}$ in a similar way to Brabec-Krausz, but instead use a scaled (dimensionless) version $\hat{D}' = (\omega_0/\beta_0)\hat{D}$ in following equations so that

$$\hat{D}' = \frac{\omega_0}{\beta_0}\left[\imath\alpha_1(\imath\partial_\tau) + \sum_{n=2}^{\infty}\frac{\gamma_n\omega_0^{n-1}}{n!}(\imath\partial_\tau)^n\right]. \tag{9}$$

Hence we get

$$\begin{aligned} 0 &= \left\{\left(\partial_\xi - \sigma\partial_\tau\right) + \frac{1}{2\imath}\left(\partial_\xi - \sigma\partial_\tau\right)^2 + \frac{1}{2\imath\beta_0^2}\nabla_\perp^2\right. \\ &\quad - \left[\imath\sigma(\imath\partial_\tau) - \frac{\imath\alpha_0}{\beta_0} + \imath\hat{D}'\right] \\ &\quad \left. + \frac{\imath}{2}\left[\imath\sigma(\imath\partial_\tau) - \frac{\imath\alpha_0}{\beta_0} + \imath\hat{D}'\right]^2\right\} A(\vec{r}_\perp,\xi,\tau) \\ &\quad + \frac{2\pi}{\imath n_0^2}(1+\imath\partial_\tau)^2 B(\vec{r}_\perp,\xi,\tau;A). \end{aligned} \tag{10}$$

This form can be rearranged without approximation to

$$\begin{aligned} &\partial_\xi A(\vec{r}_\perp,\xi,\tau) \\ &= \left(-\frac{\alpha_0}{\beta_0} + \imath\hat{D}'\right)A(\vec{r}_\perp,\xi,\tau) + \frac{\left(\imath/2\beta_0^2\right)\nabla_\perp^2}{(1+\imath\sigma\partial_\tau)}A(\vec{r}_\perp,\xi,\tau) \\ &+ \frac{2\imath\pi}{n_0^2}\frac{(1+\imath\partial_\tau)^2}{(1+\imath\sigma\partial_\tau)}B(\vec{r}_\perp,\xi,\tau;A) + \frac{T_R}{1+\imath\sigma\partial_\tau}, \end{aligned} \tag{11}$$

where

$$T_R = \left[-\frac{\imath q^2}{2}\partial_\xi^2 + \frac{\imath}{2}\left(\frac{\alpha_0}{\beta_0} - \imath\hat{D}'\right)^2\right]A(\vec{r}_\perp,\xi,\tau). \tag{12}$$

Eqn. (11) *is exact* – it contains no more approximations than our starting point eqn. (1) except for the expansion of ε in powers of ω. We recover the full field E from eqn. (4) by recombining A and knowing the carrier. The partial derivatives $(\imath\partial_\tau)$ in the denominators can, if necessary, be treated by Fourier transforming into the conjugate frequency space (Ω). Note that like τ, Ω is scaled relative to the carrier frequency.

If we set $T_R = 0$, this gives us a generalised few cycle envelope (GFEA) equation, which contains the SVEA [3], SEWA [1], and SEEA [2] within it as special cases. Of course we cannot just set the T_R term to zero without some justification, and this is discussed below.

The $\left(2\imath\pi/n_0^2\right)\mathcal{K}B$ polarization term from eqn. (11) has prefactors which depend on the time-derivative of the polarization, and these new terms are what add the effect of finite pulse lengths to the pulse evolution. Note that we can write this polarization term in different forms:

$$\begin{aligned}\mathcal{K} &= \frac{(1+\imath\partial_\tau)^2}{(1+\imath\sigma\partial_\tau)} \\ &= (1+\imath\sigma\partial_\tau)\left[1+(1-\sigma)\frac{2\imath\partial_\tau+(1+\sigma)\partial_\tau^2}{(1+\imath\sigma\partial_\tau)^2}\right] \\ &= (1+\imath\partial_\tau)\left[1+\frac{\imath(1-\sigma)\partial_\tau}{(1+\imath\sigma\partial_\tau)^2}\right]. \end{aligned} \quad (13)$$

With $\sigma = 1$, these reduce to the $\mathcal{K} = 1+\imath\partial_\tau$ SEWA [1] form. Similarly, to first order in $(\sigma-1)$, one can get the $\mathcal{K} = 1+\imath\sigma\partial_\tau$ form analogous to the SEEA corrections [2], although a strict expansion to first order in ∂_τ [13] gives a prefactor of $[1+\imath(2-\sigma)\partial_\tau]$. Finally, for a SVEA theory, $\mathcal{K} = 1$, since the ∂_τ terms are assumed to be negligible.

The T_R term is negligible if the following conditions hold:

Dispersion: terms in ∂_τ can be neglected if

$$\left|\left(\frac{\omega_0^m\gamma_m'}{\beta_0 m!}\Omega^m\right)\tilde{A}(\vec{r}_\perp,\xi,\Omega)\right| \ll \left|\tilde{A}(\vec{r}_\perp,\xi,\Omega)\right| \quad (14)$$

Evolution: terms in ∂_ξ^2 can be neglected if

$$\left|\partial_\xi\tilde{A}(\vec{r}_\perp,\xi,\Omega)\right| \ll \left|\tilde{A}(\vec{r}_\perp,\xi,\Omega)\right|, \quad (15)$$

and eqn. (15) only holds if, in addition,

Diffraction: terms in $\nabla_\perp^2$ can be neglected if

$$(1+\sigma\Omega)\beta_0^2 w_0^2 \gg 1, \quad (16)$$

Nonlinearity: is "weak" if

$$\frac{n_0^2}{2\pi}\frac{(1+\sigma\Omega)}{(1+\Omega)^2} \gg \frac{\left|\tilde{B}(\vec{r}_\perp,\xi,\Omega;A)\right|}{\left|\tilde{A}(\vec{r}_\perp,\xi,\Omega)\right|}. \quad (17)$$

We use Ω instead of $\imath\partial_\tau$ for these conditions because conditions on the frequency components of the various terms are better defined than those for time derivatives.

These conditions are the same as those required for the SEWA and SEEA theories, with the SVEA conditions being a special case gained by setting $|\Omega| \ll 1$ for the diffraction and nonlinearity conditions – implying that modulations in the envelope are so slow compared to the carrier frequency that they can be neglected. Note that backwardly propagating behaviour has not been explicitly excluded, but since it would appear as a modulation on the envelope A, it would be approximated away as part of the evolution condition (eqn. (15)).

Note that the exact solution of eqn. (11) makes no reference to a particular choice of carrier phase ψ_0. This implies that once a solution for the propagation of a particular envelope has been obtained, the problem has in fact been solved for a set of pulses (and initial conditions) based on different carrier phases – where that set is determined by the initial envelope and some arbitrary choices of carrier phase $\psi_1 \in [0, 2\pi)$. The final state is then given by the chosen ψ_1 combined with the final form of the envelope.

III. THE $\chi^{(2)}$ NONLINEAR SYSTEM

When modelling $\chi^{(2)}$ nonlinear systems we split the optical field into two or three parts, depending on whether a degenerate or non-degenerate system is being treated. For example, a parametric amplifier would have pump, signal, and idler field components. We then define an envelope A_α and carrier $e^{\imath\Xi_\alpha}$, $\Xi_\alpha = \beta_{\alpha,0}z - \omega_{\alpha,0}t + \psi_{\alpha,0}$ for each field component, and use a separate propagation equation for each. The total field is then the sum of these different components:

$$\begin{aligned} E &= E_p + E_s + E_i \\ &= A_p e^{\imath\Xi_p} + A_p^* e^{-\imath\Xi_p} + A_s e^{\imath\Xi_s} + A_s^* e^{-\imath\Xi_s} \\ &\quad + A_i e^{\imath\Xi_i} + A_i^* e^{-\imath\Xi_i} \end{aligned} \quad (18)$$

Because the wave equation eqn. (1) is linear in the electric field, we can use eqn. (18) in the theory of section II, and get a GFEA-like equation which is rather like the sum of three separate copies of eqn. (11), but with a single polarization term. In a $\chi^{(2)}$ medium this polarization term is proportional to the square of the field, and inspection of eqn. (18) shows that this can be expanded into a sum of many terms. We can then split the multiple-field GFEA equation into three separate GFEA-like equations, one for each envelope. In doing this we need to make sure to assign the pieces of the polarization term appropriately to a suitable envelope equation, whilst discarding those that are not resonant with a field carrier.

Our chosen nonlinear crystal is congruent $LiNbO_3$, for which we calculate refractive index and dispersion data from the Sellmeier equations of Jundt [14]. We model the nonlinear polarization using the square of the total electric field, retaining the parts resonant with our field carriers in the normal way. Our OPO simulations (see section V) assumed a pump frequency of 357.1 THz, with nominal signal and idler carrier frequencies of 257.5 THz and 99.6 THz respectively (wavelengths 0.84000μm, 1.16500μm, 3.0110μm). This means the pump pulse will travel through $LiNbO_3$ more slowly than the signal and it therefore needs to be injected into the crystal ahead of it (see fig. 1). When the two overlap, an idler is generated by the nonlinear interaction, and the three pulses then continue to interact with each other as they propagate through

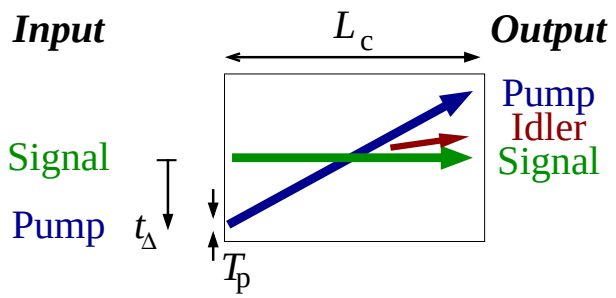


FIG. 1: Pump timing offset (see section III). The pump pulse is injected into the crystal just before the signal pulse is reflected off the input mirror. The faster moving signal pulse then catches the pump pulse up about halfway through the crystal, and an idler pulse is generated.

the crystal. Note that our ideal non-degenerate parametric amplifier simulations (see section IV) use the same field frequencies, but idealise the crystal parameters by setting the group velocities and dispersions to zero.

A. System Scalings

In a typical experiment, the crystal length would be fixed, as would any properties defined by its design, such as periodic poling. If we were to investigate this case for a range of pulse durations, there would naturally be differences between the results, even within the SVEA. For example, the relative pulse broadening caused by travelling through a 1000μm crystal is greater for a 12fs pump pulse than for a 48fs one. Similarly, a fixed timing offset for injection would have different effects; and a fixed pump pulse power would generate different strengths of nonlinear interaction for different pulse lengths. All these effects would confuse any attempt at a systematic comparison of the few cycle effects in the models we consider.

Therefore, in order to isolate specific few-cycle effects, we must scale the pump pulse FWHM $\mathcal{T}_p$, crystal length L_c, pump pulse energy $\mathcal{W}$, and pump timing offset t_Δ in such a way as to ensure the effects of group velocity, pump timing, and nonlinearity occur in the same proportions to one another over the range of pulse lengths.

We can work out an appropriate scaling by examining a simple version of the propagation equation (eqn.11), where we write the group velocity prefactors as B_1, the second order dispersion prefactors as B_2, and the polarization terms as CA^2. To assist us with the scaling process we also write $\xi = r^{-f}\xi'$, $\tau = r^{-g}\tau'$, and $A = r^h A'$, where r is the scaling factor. Our simple propagation equation is therefore

$$r^{h+f}\partial_{\xi'}A' = r^{h+g}B_1\partial_{\tau'}A' + r^{h+2g}B_2\partial^2_{\tau'}A' + r^{2h}CA'^2. \quad (19)$$

We can easily match the LHS term with the polarization term by setting $f = h$; but then we must choose either $h = g$ to match group velocities, or $f = 2g$ to match the second order dispersion – we cannot match both. For our chosen OPO situation (see section V), it is best to match the group velocity terms, which control how long the pump and signal pulses overlap – in general, the dispersion has a much smaller effect.

We take our reference situation to be a 20nJ 24fs FWHM pump pulse propagating through a 500μm crystal, with a pump timing offset of 48fs. For the chosen parameter scaling ($f = g = h$)

$$\frac{\mathcal{T}_p}{24\text{fs}} = \frac{L_c}{500\mu\text{m}} = \frac{t_\Delta}{48\text{fs}} = \frac{20\text{nJ}}{\mathcal{W}}. \quad (20)$$

This removes the gross effects caused by reducing the pulse duration, so that if there are no few cycle effects, and second order dispersion is negligible, *each pulse length should give identical results*.

First, the crystal length L_c is scaled in direct proportion to the pulse length $\mathcal{T}_p$. This means that the relative group velocities are scaled so that the pump and signal pulses spend the same relative time overlapping, leading to an equivalent nonlinear effect.

Second, and related to the previous point, the pump timing offset t_Δ is reduced in direct proportion to the crystal length (and hence pulse length). This means the pump-signal pulse cross-over occurs at the same relative point, so the effect of the pump-signal overlap is similar. If a 48fs pump pulse in a 1000μm crystal arrives 96ns before the signal, the crosover occurs at about the 500μm half-way mark – just as for a 12fs pulse in a 250μm crystal, where a $t_\Delta = 24\,fs$ gives a crossover at the 125μm half-way mark.

Third, a shorter crystal reduces the effect of the nonlinearity, so the pump pulse energy is scaled up as the inverse of the reduction in crystal length – a half length crystal needs pulse energies $\mathcal{W}$ twice as large – a 10nJ 48fs pulse in its 1000μm crystal with see the same nonlinear effect as a 20nJ 24fs pulse in its 500μm crystal. Note that the pulse energy depends on the area of the pulse, and so depends on its length, so that $\mathcal{W} \propto |A|$.

We could choose to make the scaling perfect, by also scaling the crystal parameters. If we scale the crystal dispersion with $B_2 = r^{-g}B_2'$, the relative amount of pulse spreading changes to become the same for each simulation – e.g. if the 48fs pulse widens by 10% in a 1000μm crystal, the 12fs will also widen by 10% in its 250μm crystal. We did a set of SVEA simulations on this basis, and as expected saw identical pulse profiles regardless of the chosen pulse length. However, we chose not to use this perfect scheme for the bulk of our OPO simulations because it is far from being experimentally practical.

IV. IDEAL PARAMETRIC INTERACTIONS

A parametric amplifier is a single-pass device: pump and signal pulses are injected into one end of the nonlinear crystal, they interact within it, then exit at the far end. However,

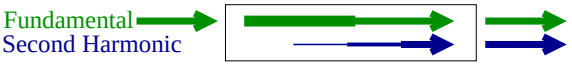


FIG. 2: SHG: Second Harmonic Generation (section IV A). The thickness of the arrows is intended to give an indication of how the energy of the field components changes during propagation through the crystal.

because real nonlinear crystals (such as $LiNbO_3$) tend to have significant dispersion, very short pulses quickly spread out, making them difficult to create, and reducing the few-cycle effects we aim to study.

In order to demonstrate clearly the nature of few-cycle effects in $\chi^{(2)}$ materials, in this section we investigate an ideal case by setting the dispersion to zero, and make the group velocity the same at all frequencies. This means that $\sigma = 1$, so the "few-cycle" polarization prefactor $\mathcal{K}$ is identical for both the SEWA and GFEA theories. Note that it is difficult to do no-dispersion simulations over long times because pulse self-steepening causes both the numerical integration and the theoretical approximations to break down.

We inject Gaussian pump and signal pulses at exactly the same time (i.e. $t_\Delta = 0$), with the same width. They then travel down the crystal with maximum overlap, interacting all the way. Other parameters are fixed by the scaling rules from section III A. Further, when *graphing* results for the figures, we scale the times for each pulse length to the 6fs case (e.g. for a 24fs pulse, "$\tau = 10$" corresponds to 40fs), and scale the pulse intensities in proportion to their initial intensities. This means that graphs of the initial conditions for a range of pulse lengths would be identical.

Finally, note that in these ideal results, the nonlinear interaction is "strong", with significant transfer of energy between the fields.

A. Second Harmonic Generation (SHG)

In second harmonic generation the nonlinearity causes a field at one frequency (the fundamental) to generate one at twice that frequency (the second harmonic). In our 48fs simulations, a 10nJ pulse is injected in at the fundamental frequency (see fig. 2).

In Figs. 4, 5 we can see comparisons of the pulses resulting from a single pass through the crystal. Although the plotted (and scaled) $|A|^2$ of the pulses are rather similar; the GFEA theory gives noticeably different results for the shortest pulses, unlike the SVEA theory. Note that the vertical scales on the two figures (not shown) are rather different.

However, this apparent similarity in $|A|^2$ is a little misleading because the underlying phase profiles of the envelopes are very different, as can be seen in (see fig. 6). More features, primarily extra oscillations, do develop at shorter pulse durations, but generally the comparisons remain similar to those shown.

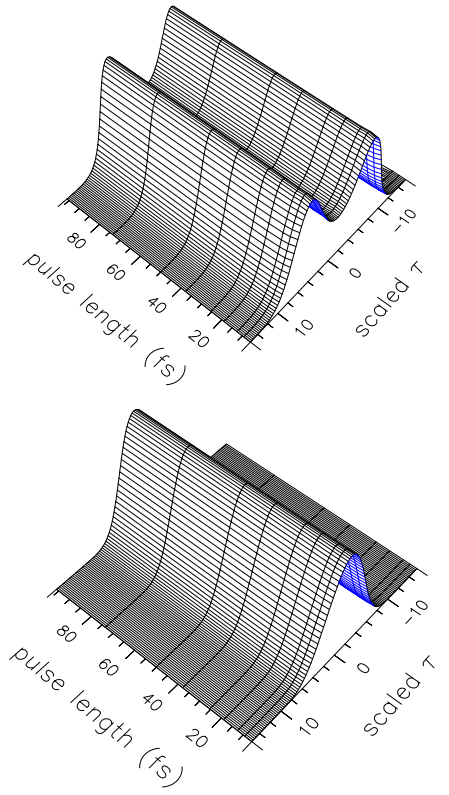


FIG. 3: SHG: Scaled pulse envelopes $|A|^2$ from the SVEA, on exit from the ideal dispersionless crystal. Top is fundamental, bottom is second harmonic.

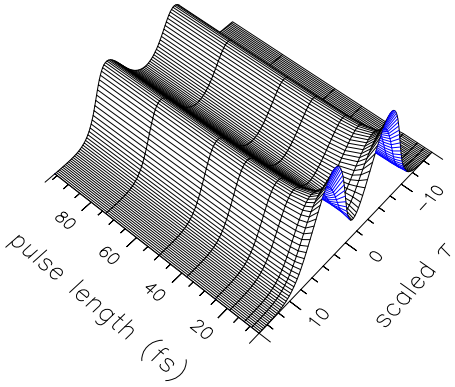


FIG. 4: SHG: Scaled fundamental pulse envelopes $|A|^2$ from the GFEA, on exit from the ideal dispersionless crystal. The SVEA results for *all* pulse lengths are essentially identical to the 96fs result.

B. Degenerate Parametric Amplification (DPA)

A degenerate parametric amplifier uses energy from a pump pulse to amplify that of a signal pulse at half the frequency ($\omega_p = 2\omega_s$, see fig. 7). For our 24fs reference simulations, a 20nJ pulse is injected at the pump frequency, and a signal pulse of 10pJ is amplified; the nonlinear interaction is very strong.

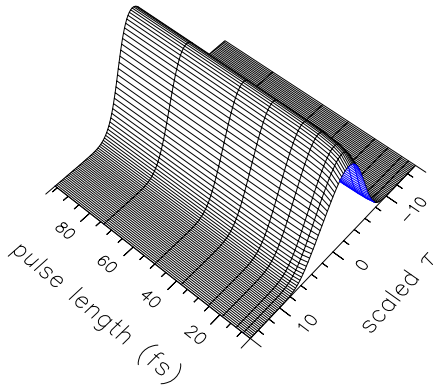


FIG. 5: SHG: Scaled second harmonic pulse envelopes from the GFEA, see fig. 4. The SVEA results for *all* pulse lengths are essentially identical to the 96fs result.

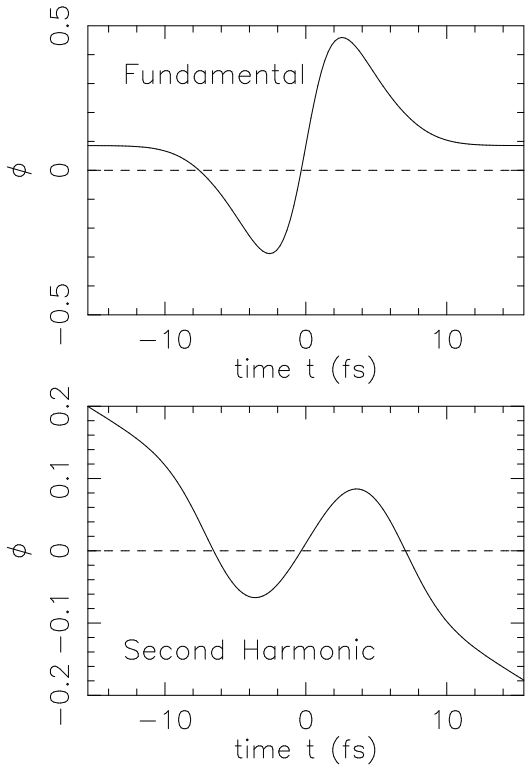


FIG. 6: SHG: envelope-phase profiles on a scaled τ, for an 18fs pulse duration. SVEA (– – –), GFEA (——). NB: the label "time t" should read "scaled τ".



FIG. 7: DPA: Degenerate Parametric Amplification (section IV B). The thickness of the arrows is intended to give an indication of how the energy of the field components changes during propagation through the crystal.

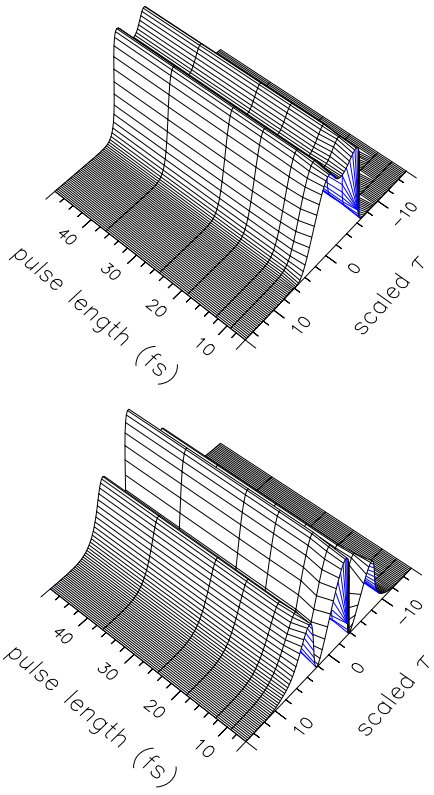


FIG. 8: DPA: Scaled pulse envelopes $|A|^2$ from the SVEA, on exit from the ideal dispersionless crystal. Top is signal, bottom is pump.

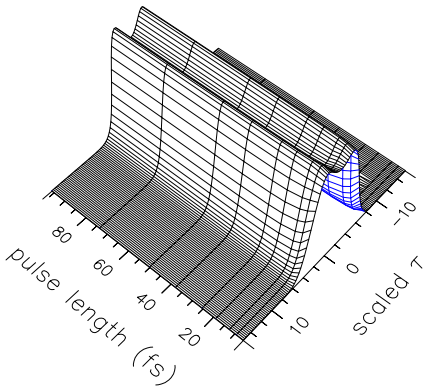


FIG. 9: DPA: Scaled signal pulse envelopes $|A|^2$ from the GFEA, on exit from the ideal dispersionless crystal. The SVEA results for *all* pulse lengths are essentially identical to the 96fs result.

In Figs. 9, 10 we can see comparisons of the pulses resulting from a single pass through the crystal. Note that the intensity profiles of the pulses are very similar, but the GFEA theory gives different results to the SVEA for the shortest pulses.

However, this apparent similarity in $|A|^2$ is a little misleading because the underlying phase profiles of the envelopes are very different, as can be seen in fig. 11. The change in phase of the pump pulse in both the SVEA and GFEA case is due to the presence of nodes that develop to either side of its cen-

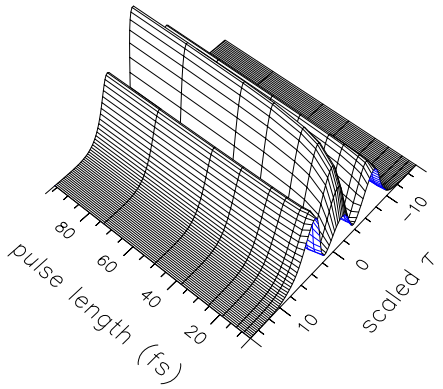


FIG. 10: DPA: Scaled pump pulse envelopes from the GFEA, see fig. 9. The SVEA results for *all* pulse lengths are essentially identical to the 96fs result.

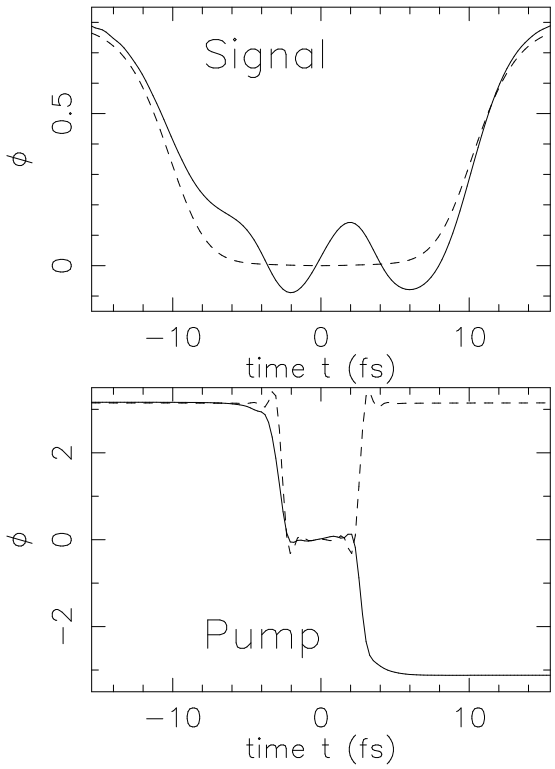


FIG. 11: DPA: envelope-phase profiles on a scaled τ, for an 18fs pulse duration. SVEA (– – –), GFEA (——). .

tre. More features, primarily extra oscillations, do develop at shorter pulse durations, but generally the comparisons remain similar.

C. Degenerate Parametric De-amplification (DPD)

This is the same situation as for degenerate parametric amplification, but we have changed the relative phase between the pump pulse and signal so that the input signal pulse is de-amplified (see fig. 12). We are interested in this case be-



FIG. 12: DPD: Degenerate Parametric De-amplification (section IV C). The thickness of the arrows is intended to give an indication of how the energy of the field components changes during propagation through the crystal.

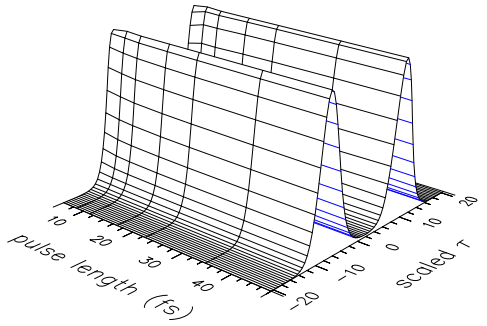


FIG. 13: DPD: Output SVEA signal intensities for $\phi_s = \pi/4$ and $\phi_p = 0$ for a range of pulse durations: peak value $|A|^2 \approx 4\times10^2$;

cause the de-amplification is very sensitive to the phase relationship between the pulses, and the few-cycles terms modify the phases of the pulses. Our SVEA model of the situation behaves in the expected way, with the signal pulse decaying away to zero as it propagates through the crystal and transfers its energy to the pump.

However the new terms in the GFEA propagation equation adjust the phases of both the pump and signal fields as they propagate, moving them away from an exact match to the de-amplification criteria. As the mismatch increases, the de-amplification process is reversed, and instead the usual am-

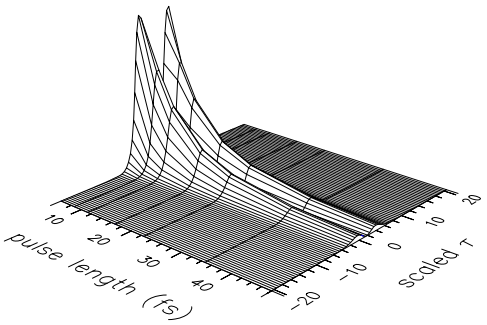


FIG. 14: DPD: Output GFEA signal intensities for $\phi_s = \pi/4$ and $\phi_p = 0$ for a range of pulse durations, peak value $\approx 4\times10^5$. The intensities and times are scaled in our usual way. The SVEA results are nearly identical for all pulse lengths, and would not show up on the scale of this GFEA graph: their output signal intensity consists of two peaks (at $\tau \approx \pm10$), with a height less than 1/30th of that of the smallest (48fs) GFEA peaks.

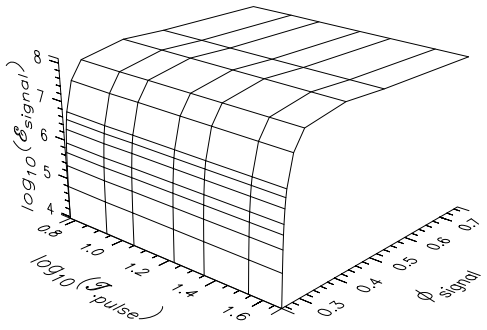


FIG. 15: DPD: Output SVEA pulse energies ($\mathcal{E}_{\rm signal} = \int |A_{\rm signal}|^2 d\tau$, arbitrary units) for a range of initial signal (envelope) phases ϕ_s and pulse lengths $\mathcal{T}_{\rm p}$.

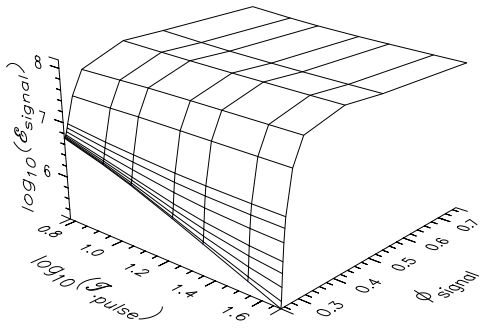


FIG. 16: DPD: Output GFEA pulse energies ($\mathcal{E}_{\rm signal} = \int |A_{\rm signal}|^2 d\tau$, arbitrary units) for a range of initial signal (envelope) phases ϕ_s and pulse lengths $\mathcal{T}_{\rm p}$. The intensities and times are scaled in our usual way. The SVEA results are nearly identical for all pulse lengths, and differ from the 48fs (i.e. $\log_{10}(48) = 1.68$) results in that the near $\phi_{\rm signal} = \pi/4$ give significantly lower energies – down to 10^4 rather than 10^5 for $\pi/4$. The graphed signal phases in multiples of π are are 0.250, 0.251, 0.252, 0.253, 0.254, 0.256, 0.258, 0.260, 0.275, 0.300, 0.400, ..., 2.000

plification takes over. Fig. 14 shows the output signal pulse profiles on exit from the crystal, note the enormous difference in the few-cycle dependence of the SVEA and GFEA theories – both in character and amplitude. The SVEA profile is just the residual input signal pulse which has not yet been fully "de-amplified"; this residue can also be seen as a shoulder on the wings of the GFEA profiles if plotted on a log scale. The large and very visible double peak in the GFEA graph is a result of the finite pulse length on the nonlinear polarizations term – as can be seen in eqn. (13), this alters the phase profile of the nonlinear effect, and hence the pulses, which means the signal no longer satisfies the exact criteria for de-amplification. For our chosen input pulse powers, this effect persists for initial phase mismatches up to ~ 0.01 radians, after which the amplification of the signal pulse has largely swamped the anisotropy induced by the few-cycle effects. Of course the effect is most visible when the interaction has been strong enough for the input component of the signal pulse to (almost) completely disappear.

In fig. 16 we see how the behaviour changes both with pulse length and initial phase match – we see perfect de-amplification in the SVEA model, but the steeply sloping $\phi_{\rm signal} = \pi/4$ line clearly demonstrates the effects of a finite pulse length. Of course as the $\phi_{\rm signal}$ moves further from $\pi/4$, the SVEA model no longer undergoes perfect de-amplification, and so the difference between the two models becomes small.

D. Non-degenerate Parametric Amplification (NPA)

We consider first a non-degenerate parametric amplifier with pump, signal, and idler frequencies such that $\omega_p \to \omega_s + \omega_i$, and $\omega_s \neq \omega_i$. In the 24fs reference case, the initial pump energy is 20nJ and the initial signal energy is 10pJ, with a negligible (but finite) idler. For other pulse durations, the energies were scaled according to eqn. (20). Fig. 17 shows how, according to the GFEA, the idler pulse intensity profiles $|A_i|^2$ generated in a single pass of the crystal vary with pulse

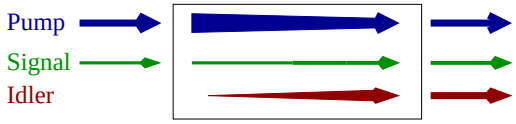


FIG. 17: NPA: Non-degenerate Parametric Amplification (section IV D). The thickness of the arrows is intended to give an indication of how the energy of the field components changes during propagation through the crystal.

duration. The profiles show little variation with pulse duration except for the shortest pulses ($\tau \lesssim 20$), where distortion is evident; the signal and pump profiles show deviations of a comparable magnitude.

In fig. 19, 20, 21 we can see equivalent comparisons for the signal and pump intensity profiles.

More dramatic effects appear in the phase profiles: in fig. 22, the phases of the pulse envelopes at pulse durations of 18fs and 96fs are shown with the phase distortions due to the finite pulse lengths (see eqn. (13)). As the pulse duration shortens, the principal effect is to increase the magnitude of the phase distortion, leaving the shape of each profile largely unchanged; however more complex phase oscillations develop for the shortest pulses. At 96fs, the profiles show a smaller distortion, and are tending towards the long-pulse SVEA limit. In this limit, the profiles are essentially flat, although the pump field develops nodes which give rise to a step-like change in the phase.

E. Non-degenerate Parametric De-amplification (NPD)

As a variant on the case just treated, signal and idler pulses with equal numbers of photons were injected, and the rela-

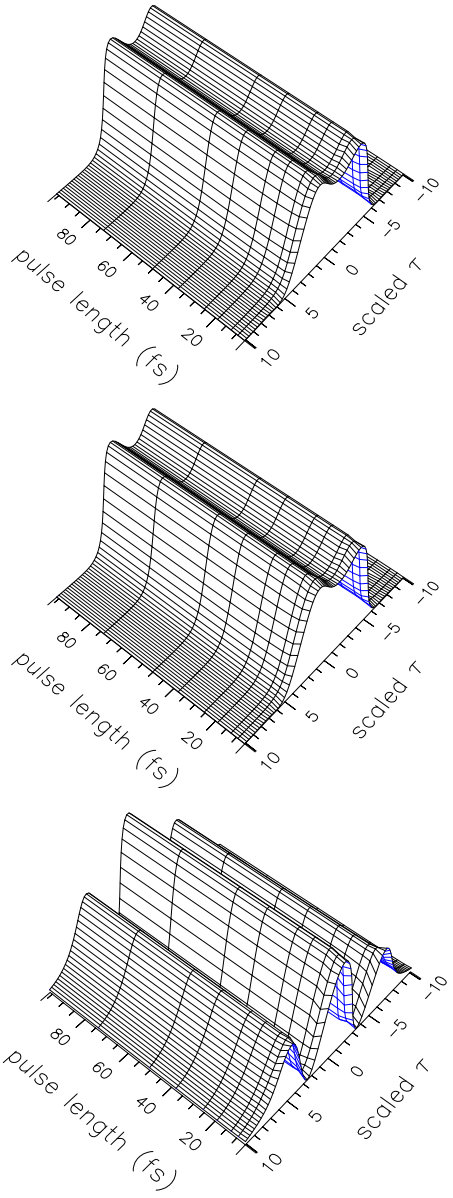


FIG. 18: NPA: Scaled SVEA pulse envelopes $|A|^2$ on exit from the ideal dispersionless crystal. Top to bottom is idler, signal, pump.

tive phases of the pulses set to ensure that the signal and idler experience initial de-amplification (see fig. 23). Since the subsequent evolution is sensitive to phase changes, and the finite pulse length terms in the GFEA affect the phases, this is an interesting situation to examine. In the SVEA, the signal and idler decay away towards zero as the pulses propagate, so the SVEA output signal is just some residual part of the input. The GFEA evolution is different, as can be seen from eqn. (13) – the finite pulse lengths alter the phase profile of the nonlinearity, and hence change the evolution of the pulses. During an initial period of de-amplification, the pulses undergo a gradual phase distortion. Then, as the discrepancy increases, amplification takes over. In a comparison of SVEA and GFEA models, the effect caused by the phase distortion

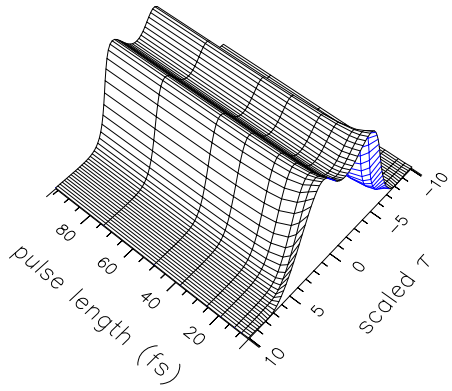


FIG. 19: NPA: Scaled GFEA idler pulse envelopes $|A|^2$ on exit from the ideal dispersionless crystal. The SVEA results for *all* pulse lengths are essentially identical to the 96fs result.

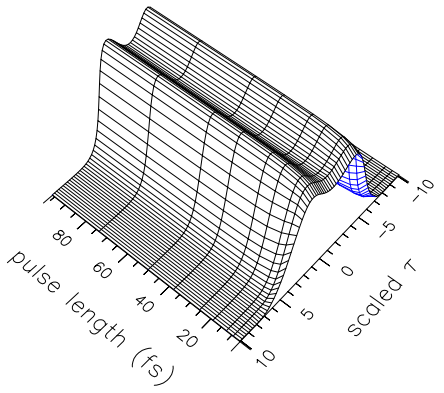


FIG. 20: NPA: Scaled GFEA signal pulse envelopes, see fig. 19. The SVEA results for *all* pulse lengths are essentially identical to the 96fs result.

is more visible when the interaction is been strong enough for the input component of the signal pulse to be strongly depleted, and also is much stronger for shorter pulses

The GFEA signal pulse profiles on exit from the crystal as a function of pulse duration are presented in fig. 25. Note that the SVEA prediction corresponds to the long-pulse limit of the GFEA figure, but those limiting features are too small to be seen.

The double peak is a result of the finite pulse length on the nonlinear polarization – the "phase twist" caused by the few cycle terms is odd, causing a node at $\tau = 0$ as the field is amplified – at exactly $\tau = 0$, the field continues to be de-amplified. Note that at 18fs, for example, the output signal pulse amplitude is larger than the input value.

The SVEA profile in fig. 24 is just the residual input signal pulse which has not yet been fully "de-amplified"; this residue can also be seen as a shoulder on the wings of the GFEA profiles if plotted on a log scale. Fig. 25 shows the output GFEA signal pulse profiles on exit from the crystal, note the enormous difference in the few-cycle dependence of the SVEA and GFEA theories – both in character and amplitude.

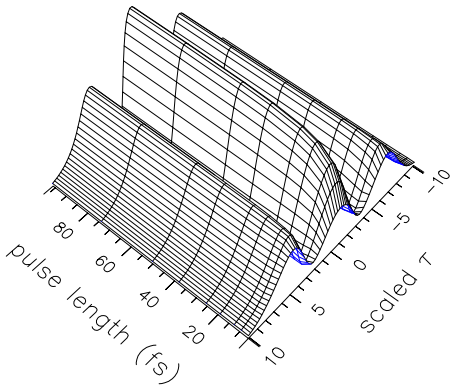


FIG. 21: NPA: Scaled GFEA pump pulse envelopes, see fig. 19. The SVEA results for *all* pulse lengths are essentially identical to the 96fs result.

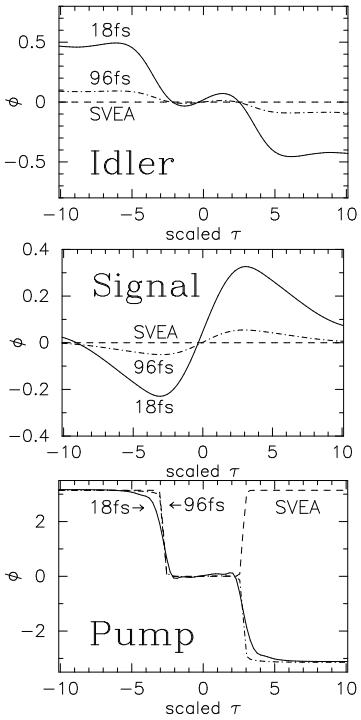


FIG. 22: NPA: envelope-phase profiles for 18 and 96fs pulse durations. Top to bottom: idler, signal, pump; SVEA (– – –), GFEA 96fs (–·–·–·–), GFEA 18fs (——).

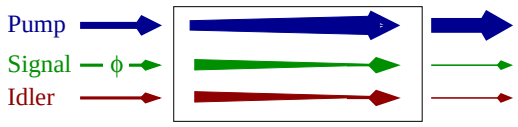


FIG. 23: NPD: Non-degenerate Parametric De-amplification (section IV E). The thickness of the arrows is intended to give an indication of how the energy of the field components changes during propagation through the crystal.

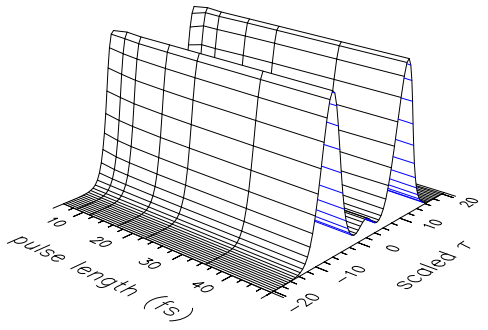


FIG. 24: NPD: Output SVEA signal intensities for $\phi_s = \pi/4$ and $\phi_p = 0$ for a range of pulse durations: peak value $|A|^2 \approx 4\times10^2$).

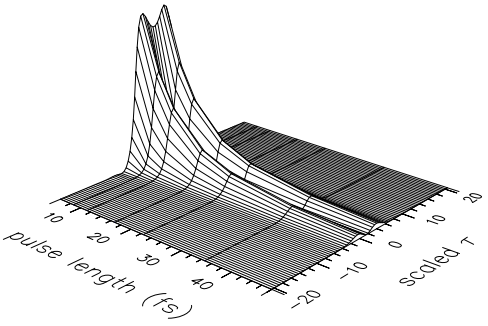


FIG. 25: NPD: Output GFEA signal intensities for $\phi_s = \pi/4$ and $\phi_p = 0$ for a range of pulse durations, peak value $\approx 6\times10^5$. Equivalent SVEA results are very different: they are the same for all pulse lengths, are too small to show up on the scale of this graph (being ∼3% of the height of the 48fs GFEA peaks), and the two peaks are located further from the origin (at $\tau \approx \pm10$).

In fig. 26 we see how the SVEA behaviour changes both with pulse length and initial phase – here we see perfect de-amplification.

The GFEA output pulse energies are displayed in fig. 27, which shows how the behaviour changes both with pulse length and initial phase. The data for $\phi_{\text{signal}} = \pi/2$ demonstrates the effects of exact initial conditions and finite pulse length; maximum de-amplification occurs in the long-pulse (SVEA) limit. If we instead start with a signal phase slightly different from $\pi/2$, e.g. 0.51π, the de-amplification is less efficient and will eventually be overtaken by the amplification, even for the SVEA model. Consequently, comparisons for imperfect initial phases are dependent on the length of the crystal. However, since we use a scaling procedure, the results still behave in a systematic way, even if they are not completely generic.

Of course, changing other initial conditions can also disturb the de-amplification: e.g. different numbers of signal and idler photons. Although both signal and idler will initially be de-amplified, as they approach zero photon number, one field will "overshoot" the zero and be inverted. This alters the phase

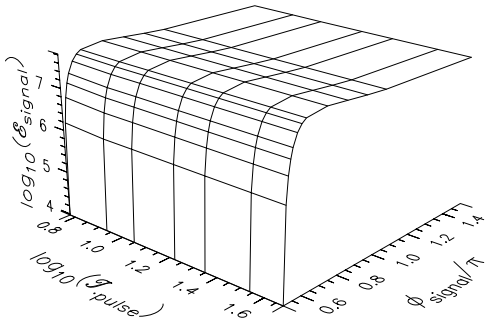


FIG. 26: NPD: Output SVEA pulse energies ($\mathcal{E}_{\rm signal} = \int |A_{\rm signal}|^2 d\tau$, arbitrary units) for a range of initial signal (envelope) phases ϕ_s and pulse lengths $\mathcal{T}_{\rm pulse}$.

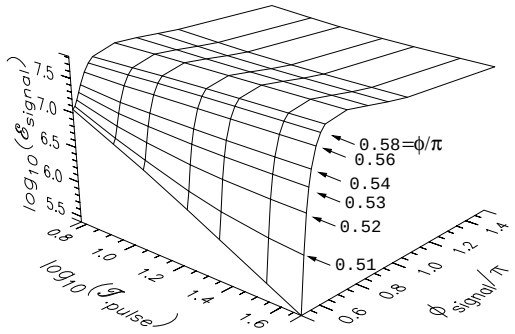


FIG. 27: NPD: Output GFEA pulse energies ($\mathcal{E}_{\rm signal} = \int |A_{\rm signal}|^2 d\tau$, arbitrary units) for a range of initial signal (envelope) phases ϕ_s and pulse lengths $\mathcal{T}_{\rm pulse}$. The intensities and times are scaled in our usual way. The SVEA results are nearly identical for all pulse lengths, and differ from the 48fs (i.e. $\log_{10}(48) = 1.68$) results in that the near $\phi_{\rm signal} = \pi/2$ give significantly lower energies – down to 10^4 rather than 3×10^5 for $\pi/2$.

relationships, and so again amplification takes over. As an example, simulations based on our 18fs pulses suggested that photon number mismatches of about one percent would not noticeably disrupt the appearance of either fig. 25 or 27.

These comparisons testing the sensitivity of these results to mismatches in the initial conditions are of course dependent on our chosen system parameters. For example, either more intense pulses or longer crystals would diminish the difference between SVEA and GFEA predictions; conversely, weaker pulses or shorter crystals would enhance them.

V. OPTICAL PARAMETRIC OSCILLATION (OPO)

We move on from optical parametric amplification to a synchronously-pumped Optical Parametric Oscillator (OPO). As shown in fig. 28, we considered the case of a $LiNbO_3$ crystal in an optical cavity with mirrors that reflect the signal wavelength only. The oscillator is driven by a train of gaussian pump pulses whose periodicity closely matches the natural period of the cavity, and which amplify and then sustain the signal pulse confined within it. The cavity length can be "tuned" about exact synchronisation. The idler pulse, generated when the signal pulse interacts with each new pump pulse, is transmitted through the output mirror with the pump, while the signal is strongly reflected. For a given set of parameter values, we modelled the development of the signal pulse over many cavity transits until it reached a steady state. Typically, we found that the signal stabilised in several hundred transits although, in a few cases, no equilibrium was achieved and the system oscillated indefinitely. We studied the evolution for a range of phase-matching conditions ($\Delta k = 0$ to $24\times10^{-3}/\mu$m, and cavity length tunings (-16fs to $+16$fs). Except where stated, the figures contain data for the perfectly phase matched and sychronised case.

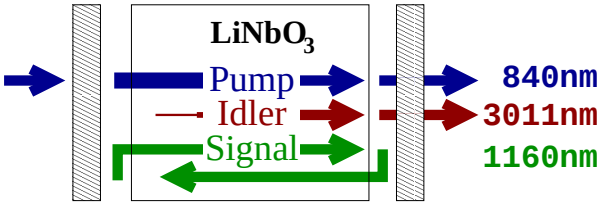


FIG. 28: Simplifed optical parametric oscillator experiment set-up (see section V).

The steady state was determined by propagating the pulses through many passes of the oscillator until the modulus-squared of the pulse *envelopes* had stabilized.

A. Dispersion Scaled OPO

As discussed in section III A, it is possible to make the SVEA propagation equation completely scale invariant if we modify the crystal dispersion parameters as well as the pulse length, energy, and crystal length. Although this is not an experimentally achievable goal, it is instructive to look at what happens to the OPO output in this instance. To make automatic processing of the results more convenient, we adjusted the crystal lengths to be exact powers of two, which differed slightly from those derived from the standard reference length: i.e. the 24fs pulse case related to a crystal length of 512μm, not 500μm. As expected from the scaling, and shown on figs. 29, 30, the scaled SVEA results were independent of pulse length.

In contrast the GFEA pulse profiles have a more complex behaviour, as shown on figs. 31, 32. For the chosen parameters, they have a profile which becomes increasingly distorted at shorter pulses; but there is also an abrupt transition to what is an SVEA-like pulse profile at between 36 and 48fs.

On fig. 33 we can see this transition and the expected gradually convergence of GFEA and SVEA; the maximum differ-

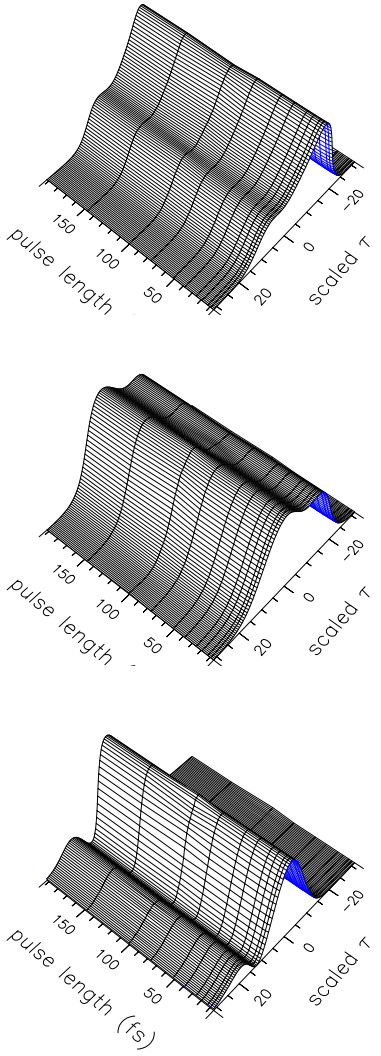


FIG. 29: Dispersion Scaled OPO: Time domain representation of the SVEA modulus-squared of the pulse envelopes, for a range of injected pump pulse durations: 6-192fs. (bottom to top) pump, signal, and idler.

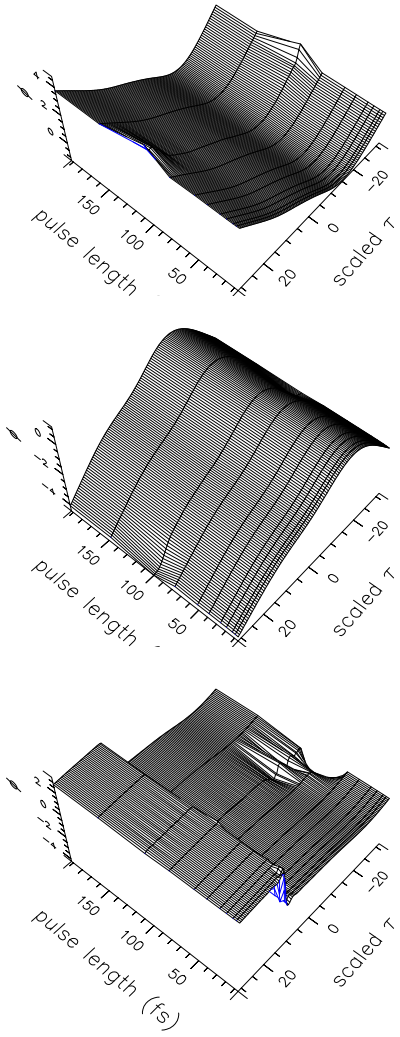


FIG. 30: Dispersion Scaled OPO: Time domain representation of the SVEA amplitude phase, for a range of injected pump pulse durations: 6-192fs. (bottom to top) pump, signal, and idler.

ences plotted are about 10% of the pulse heights, this message is repeated on fig. 34. If the convergence of GFEA to SVEA seems slower than inutitively expected, this could be partly explained by noting that the effect of the extra ∂_τ term caused by the non slowly-varying nature of the pulses has less distance over which to accumulate, so a similar discrepancy between SVEA and SEWA at e.g. 24fs and 12fs means that the 12fs case accumulates additional evolution at twice the rate as at 24fs – as indeed is to be expected, since broadly speaking, the time derivative of a pulse envelope will double as its pulse length is halved.

Note: the slight disruption to the wings of the 92fs results are because the time width allowed for by the simulation is smaller when compared to the pulse width for this particular case.

B. Scaled OPO

The complex nature of the dynamics, which arises from repetitive cycling of the signal pulse in the presence of many interacting processes makes the isolation and analysis of few-cycle effects within the different models quite complicated. Fig. 35 shows intensity profiles for the pump, signal, and idler (bottom to top in each frame) for the SVEA (dashed line) and GFEA (solid line) for four different pulse durations. Simulations with pump pulse durations of 48fs and over never reached a steady state, and so are not included here. The first point to note in fig. 35 is that the SVEA results are not identical in all frames, even though the scaling procedure in section III A is designed to make them, as far as possible, *independent* of pulse duration. The reason is that, as noted in section III A, the dispersion scales in a different way to the group time delay, and so is not correctly compensated by eqn. (20).

A second rather surprising feature is that we might expect

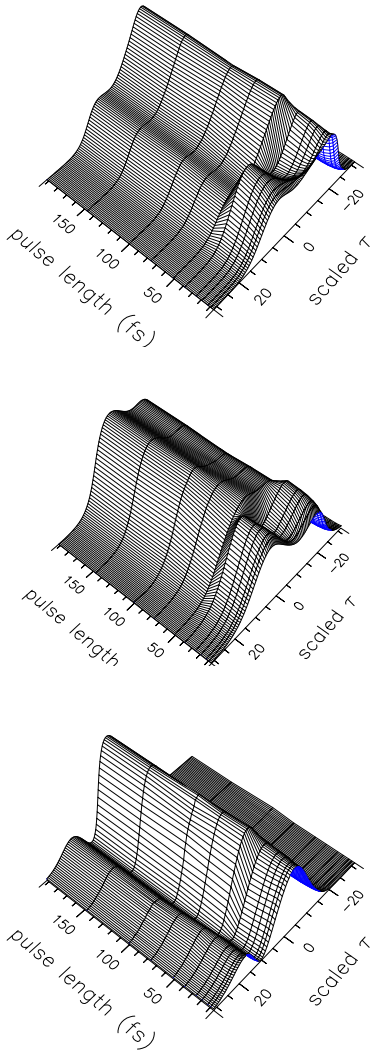


FIG. 31: Dispersion Scaled OPO: Time domain representation of the GFEA modulus-squared of the pulse envelopes, for a range of injected pump pulse durations: 6-192fs. (bottom to top) pump, signal, and idler.

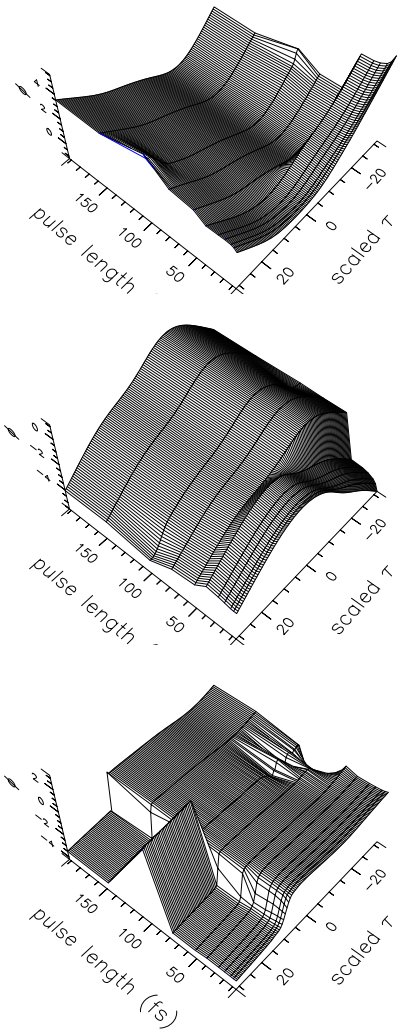


FIG. 32: Dispersion Scaled OPO: Time domain representation of the GFEA amplitude phase, for a range of injected pump pulse durations: 6-192fs. (bottom to top) pump, signal, and idler.

the GFEA results to tend to the SVEA as pulse length increases, but this is not evident from the graphs. The explanation for this is that the steady state of the OPO can change suddenly as the parameters are varied. This property is highlighted in fig. 31, which shows the GFEA signal pulse profile for pulse durations from 6fs to 192fs; the sudden adjustment of the GFEA when moving from 36fs to 48fs takes it close to the SVEA, and the difference between the two gradually disappears as the pulse duration is increased further (see Fig. 34). Note that the scaling procedure used for fig. 31 is an extension of eqn. (20) in that the dispersion term is also scaled, making the SVEA results completely independent of pulse duration.

Spectral profiles corresponding to the temporal profiles of fig. 35 and 36 are shown in fig. 37. The spectral shape for each field is similar across all pulse durations, with a pulse of double the (time) width naturally having half the bandwidth. Notice that the pump and signal spectra in the 6fs frame are close to overlapping, which indicates that the separation of the total EM field into distinct pump, signal, and idler components is becoming a questionable assumption.

Inclusion of the carrier wave in the results raises some quite subtle issues that need careful consideration. It must be stressed again that the carrier drops out of the analysis leading to eqn. (11). The envelope description is therefore complete, although the phases of two of the three envelope functions can be changed by arbitrary constants without any effect on the computations apart from an appropriate adjustment in the phase of the third envelope. For instance, if the phases of the pump and signal envelopes are changed by $\Delta\phi_p$ and $\Delta\phi_s$, the phase of the idler envelope is changed by $\Delta\phi_i = \Delta\phi_p - \Delta\phi_s$. Adjustments of this kind show up in the results only if graphs of the complete electric field profiles, including the carrier waves, are displayed, as in fig. 38. If the simulations in that figure were re-run with differing envelope phases, this would

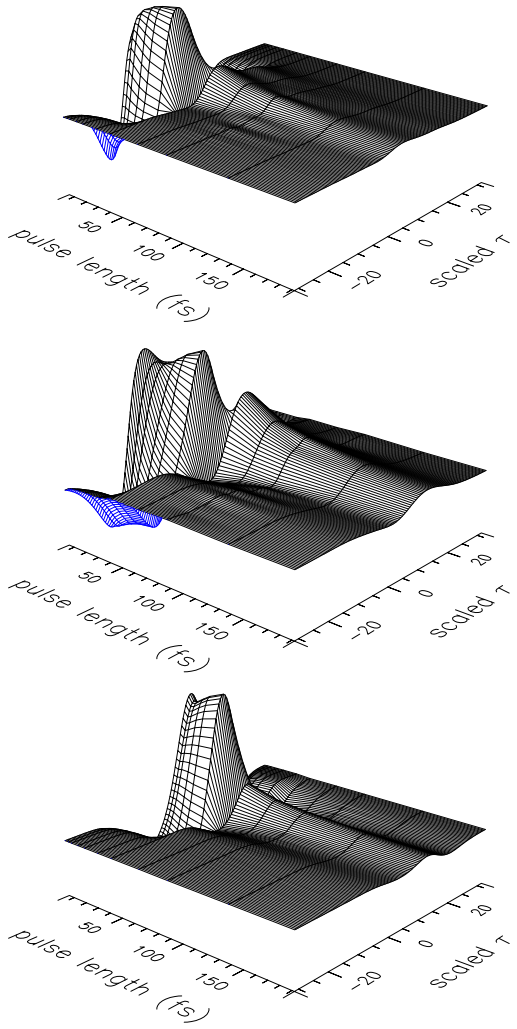


FIG. 33: Dispersion Scaled OPO: Time domain representation of the difference between the modulus-squared of the pulse envelopes between SVEA and GFEA theories, for a range of injected pump pulse durations: 6-192fs. (bottom to top) pump, signal, and idler.

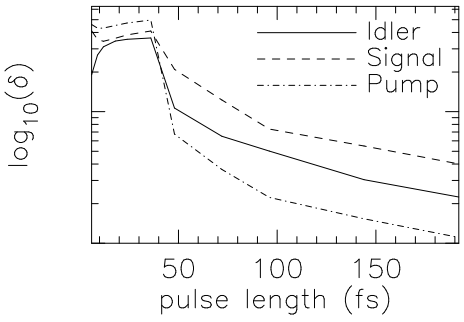


FIG. 34: Dispersion Scaled OPO: Maximum difference δ between GFEA and SVEA simulations over the middle quarter of the scaled τ range, on a $\log_{10}$ scale.

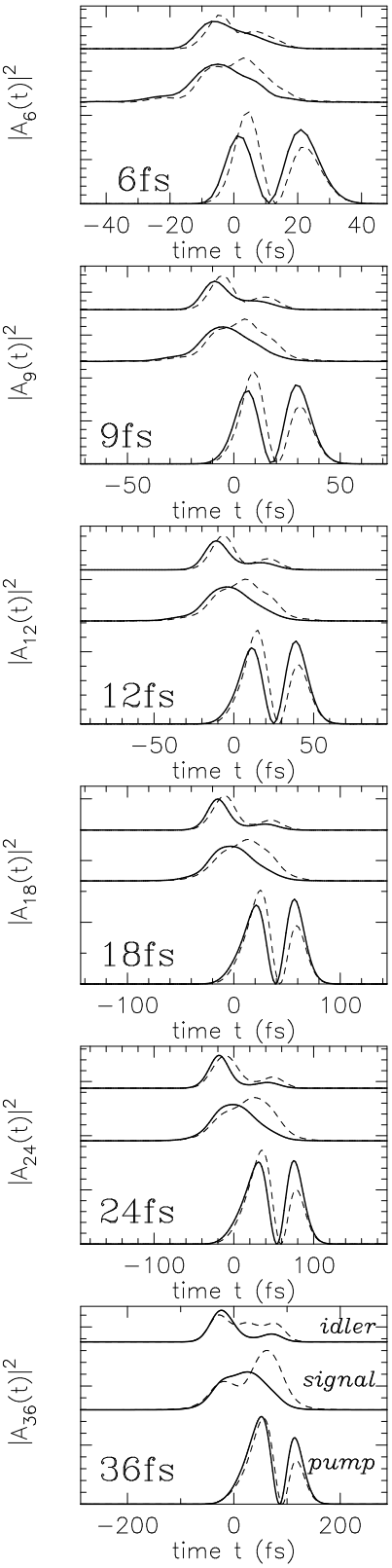


FIG. 35: Scaled OPO: Time domain representation of the modulus-squared of the pulse envelopes, for a range of injected pump pulse durations: 6fs (top), 9, 12, 18, 24, 36fs (bottom). For each subfigure, the curves compare (bottom to top) pump, signal, and idler for the SVEA simulations (– – –) and GFEA ones (——).

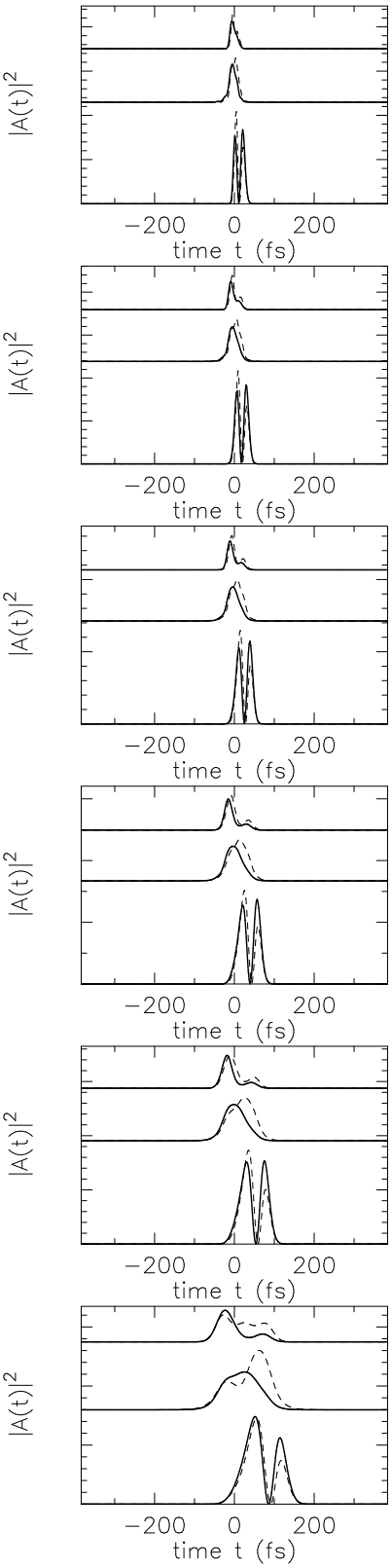


FIG. 36: Scaled OPO: As above in fig. 35, for 6fs (top), 9, 12, 18, 24, 36fs (bottom); but using the same time window width for all pulse widths.

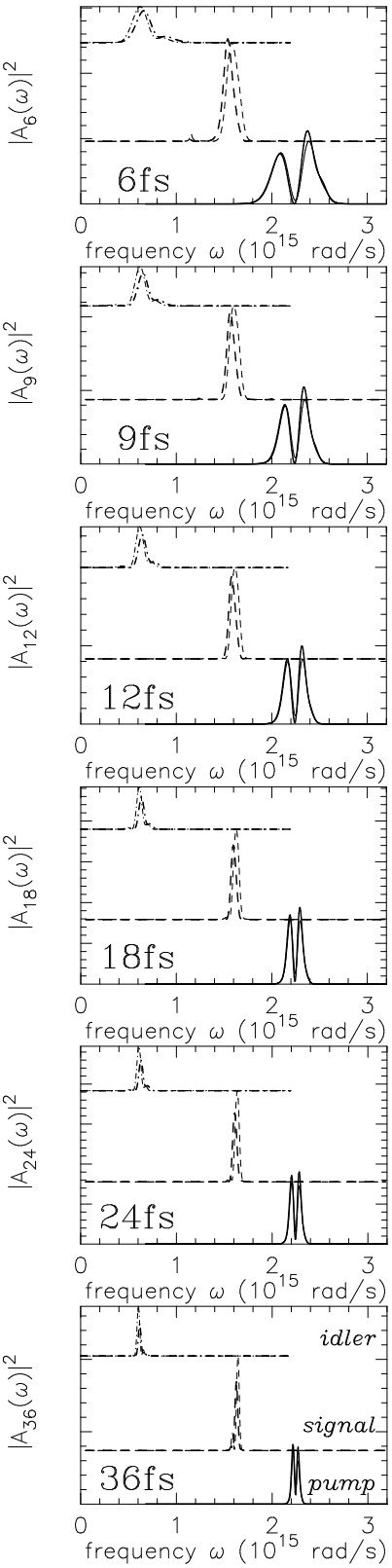


FIG. 37: Scaled OPO: Frequency domain representation of the modulus-squared of the pulse envelopes, for pump pulse durations of 6, 12, 18, 24, and 36fs. For each sub-figure, the curves compare (bottom to top) pump, signal, and idler for the SVEA simulations (– – –) and GFEA ones (——).

be reflected in temporal displacements of the carrier-like oscillations beneath the envelopes.

A further interesting feature is that, while the moduli of the pulse enveleopes may have stabilised in a simulation, the envelope phases can (and usually do) change from pass to pass; this process continues indefinitely, so a movie made up of frames from successive transits would show the pump, signal, and idler electric field oscillations drifting across underneath the respective steady envelope profiles.

Note that although it is common to talk of "shifts in carrier phase", in the theory *the carrier phase is specified by the initial conditions, and does not change.* The effects usually ascribed to "shifts in carrier phase" instead manifest themselves as a shift in the phase of the complex envelope.

The different models discussed in this paper give significantly different results for the pass-to-pass phase drift. Fig. 39 shows the phase change for the signal pulses as a function of pulse length for the SVEA, SEWA, and GFEA; note that the SEWA and GFEA results are similar to each other, while the (less accurate) SVEA exhibits a very different dependence.

The reference point used in calculating the phase drift is at the maximum amplitude of the envelope of the signal pulse, which is in fact not necessarily at the point of maximum electric field. This is a good choice for our purposes because it does not move between passes once a steady state is established. Although these phase drifts are quite small, discrepancies between the SVEA and GFEA will quickly accumulate.

Analysis shows that the phase of the envelope at this reference changes by a fixed amount from one pass to the next. Since this phase drift tends to be small, a slow evolution of the E field profile can be seen between passes in any given simulation. Further, the accumulated difference between the less accurate SVEA prediction and the GFEA can lead to large differences in the predicted electric field profiles, even if the envelope profiles happened to be similar. Note that the idler pulse envelope phase drift is in the opposite direction to the signal drift, since the pump pulse arrives with the same envelope phase at the beginning of each pass.

The details of fig. 39 are less important than its message. Getting an output of either an identical idler pulse from pass to pass or at least a well understood pulse shape progression can be important, and this will be achieved using accurate models or by experiment based on accurate models. We see that even for relatively long pulses the SVEA theory predicts a different phase drift to that of the SEWA/GFEA theory; and that the trend is different even when using a sequence of parameters designed to minimise the differences between simulations of different pulse lengths.

C. Synchronisation and Phase Mismatch

The phase drift varies as a function of the phase mismatch and the cavity synchronisation: the data is shown in Figs. 40, 41. The glitches in the data are caused by occasional difficulties in evaluating the phase of the envelopes and the wide variations that can occur for near-zero fields – not all the data

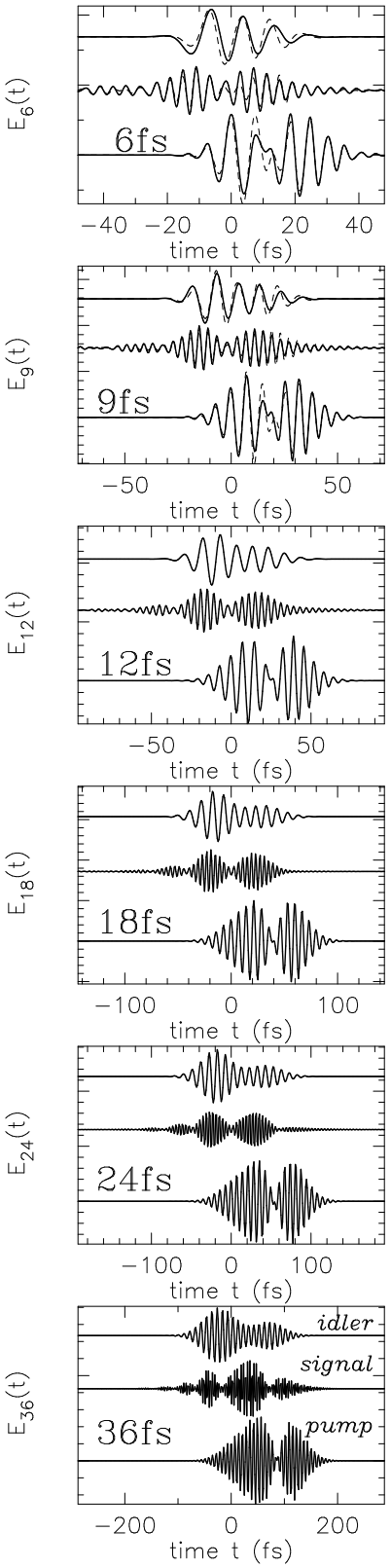


FIG. 38: Scaled OPO: Time domain representation of the electric fields of the pulse, for pump pulse durations of 6, 12, 18, 14, and 36fs. For each sub-figure, the solid curves (——) compare (bottom to top) pump, signal, and idler for the GFEA simulations, for 6fs and 9fs the SVEA fields are also indicated (– – –). The phases are chosen so that the maximum excursion of the signal envelope is purely real valued, and the idler phase is chosen so that $\phi_s + \phi_i = \phi_p$.

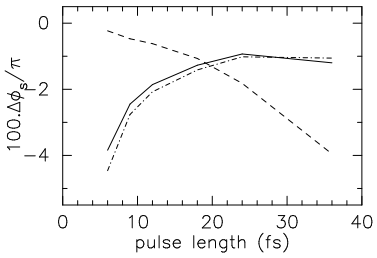


FIG. 39: Scaled OPO: Pass-to-pass phase drift for a range of parameters, comparing SVEA (– – –), GFEA (——), and SEWA (–·–·–·) simulation results. The differences are taken between the phase at the peak of the modulus-squared of the envelopes at the end of one pass of the signal pulse and the next.

points represent good steady states.

D. Fixed Length Crystal

Here we present results for a more realistic case of a fixed length crystal (1000μm) and a range of pump pulse durations (6 – 96fs); with all parameters being kept constant, notably a fixed pulse energy. Since the crystal is relatively long, the high dispersion comes into play, ensuring that even for rather short pump pulses (e.g. 6fs), the signal and idler become relatively broad ($\sim$ 200fs) – thus the role of few-cycle effects should be relatively small. However, inspection of the envelope profiles for the SVEA and GFEA models still show small but noticeable differences, for both perfect and imperfect phase matching, even for pump pulses as long as 96fs.

In fig. 42 we see how the inter-pass phase difference for the signal (and hence idler) for a fixed 1000μm crystal with decreasing pump pulse widths and adjusted time offsets, but fixed pulse energy. Difference between the SVEA predicted phase drift and the GFEA are noteable for perfect phase matching ($\Delta k = 0$), but when this is no longer exact, the two predictions rapidly become similar, as now both a long crystal and imperfect phase matching both act against the generation of clear few cycle effects.

VI. CONCLUSIONS

We have presented a new and more complete derivation of how the envelopes of extremely short optical pulses evolve in nonlinear interactions. We have compared the results of our new (GFEA) model to those of the traditional slowly varying envelope approximation (SVEA) using a scaling procedure to distinguish specific few-cycle effects from other phenomena caused by changing pulse duration. It should be noted that the SVEA becomes inadequate whenever the envelope changes rapidly within a few carrier periods. Strictly speaking, a few-cycle pulse is not required, because a steep edge within a longer pulse also fulfils the conditions.

The effect of the extra "few-cycle" terms in the GFEA evo-

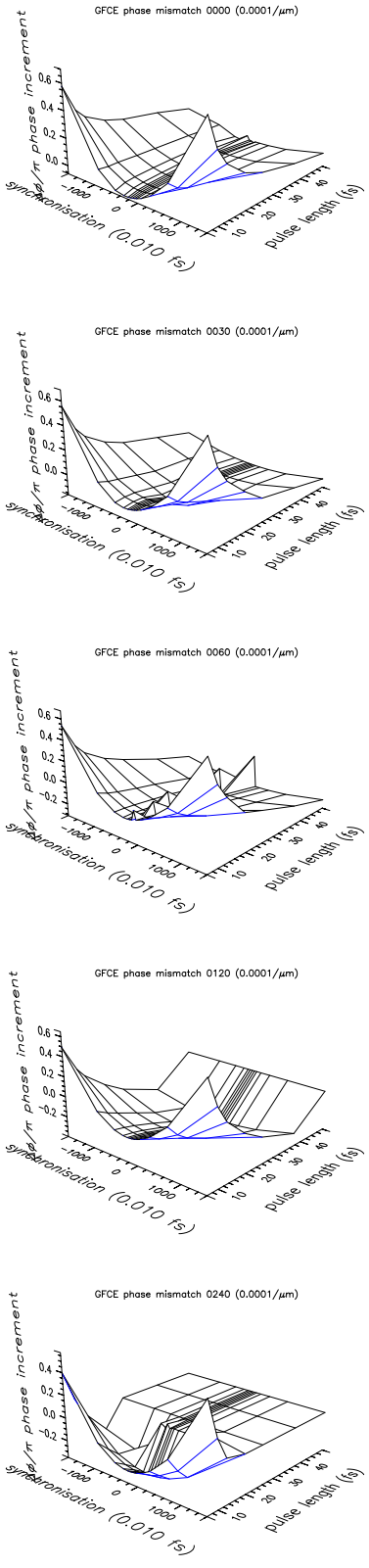


FIG. 40: Scaled OPO: GFEA phase mismatch vs sync

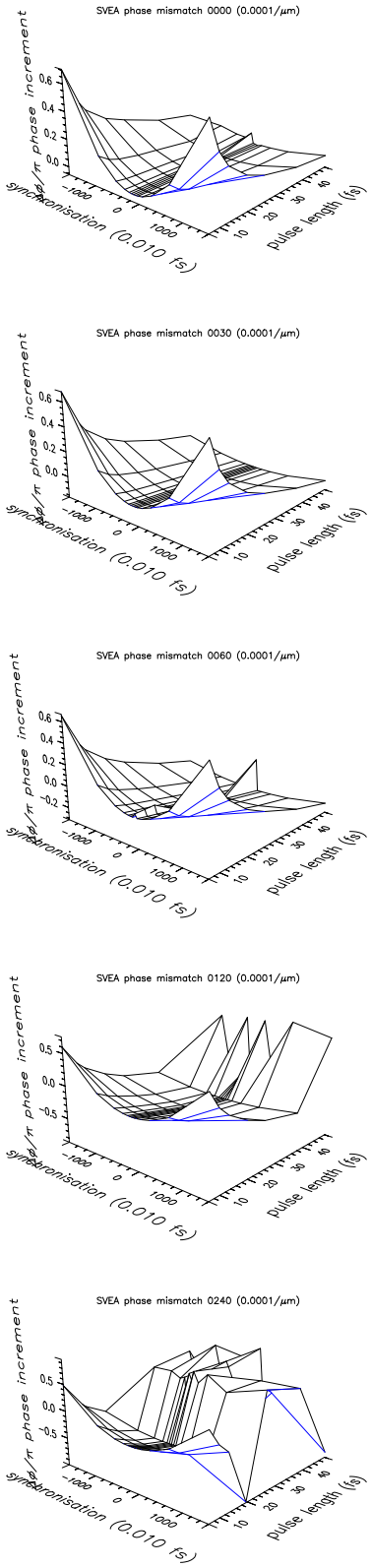


FIG. 41: Scaled OPO: SVEA phase mismatch vs sync

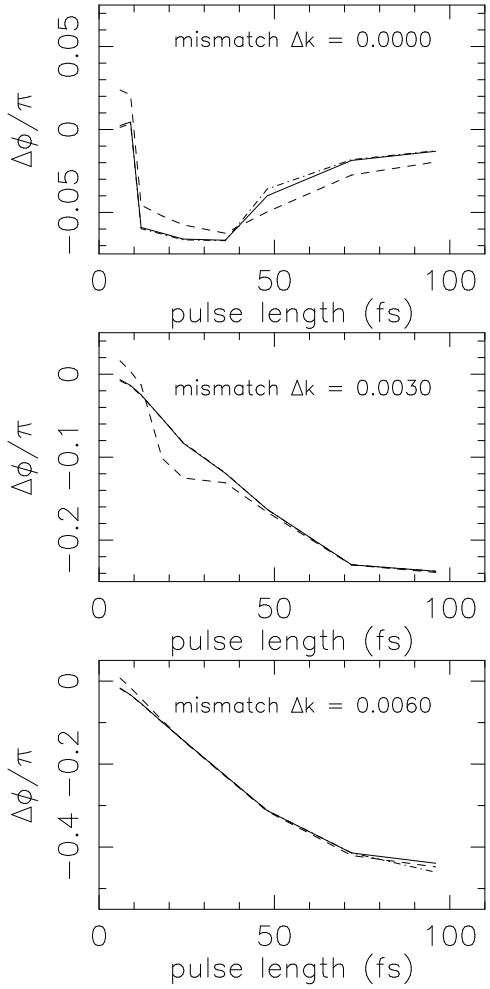


FIG. 42: 1000μm OPO: Pass-to-pass phase drifts for a differing pulse lengths but a fixed crystal length of 1000μm and equal pulse energies, comparing SVEA (——), SEWA (– – –), and GFEA (–·–·–·) simulation results. The differences are taken between the phase at the peak of the modulus-squared of the envelopes at the end of one pass of the signal pulse and the next. Each graph is for a different phase mismatch Δk in the periodic poling of the crystal.

lution equation is to add a phase distortion to the nonlinear polarization term, which then imposes itself on the pulse envelopes. This is demonstrated by our single-pass optical parametric amplifier NPA model where, whilst the SVEA model is insensitive to pulse length, the GFEA theory shows clear changes as the pulses get shorter and contain fewer optical cycles.

Further, when we studied the highly sensitive de-amplification case (i.e. NPD), we saw dramatic differences between the SVEA and GFEA simulations even outside the few-cycle regime. These arose from the phase distorting effects of the few-cycle terms in the theory disrupting the exact phase relationships needed for de-amplification. While the absolute size of these differences do depend on the chosen parameters of crystal length, pulse energy, and so on, they will always get dramatically larger for shorter pulses,

On the other hand, the repetitive cycling nature of the op-

tical parametric oscillator (OPO) produces more complicated and subtle dynamics; small changes in parameter values can, for instance, cause sudden changes in the steady state fields. It is therefore no surprise that comparison of the results predicted by the different models is less straightforward in the OPO case. The new model certainly produces differences in the pulse envelopes as well as the phases, although the way in which the GFEA tends to the SVEA in the long-pulse limit has some interesting features. The two models also predict different results for the pass-to-pass phase drift of OPO pulses, and this implies significant differences in the electric field structures. In both cases, the carrier wave moves under the envelope from one transit to the next, but by different amounts.

It can be useful to regard these "few-cycle" effects as adding a phase twist to the envelope evolution. This then shows itself most clearly in the pass-to-pass phase drift in the signal and idler phases (see Fig. 39). Finally, although these effects are usually described as "few-cycle effects", they are more accurately described as "finite pulse length" effects. Although for the parameter ranges needed to describe typical nonlinear crystals, it is only in a few-cycle regime where the effects are easily visible in the pulse intensity profiles, these twisting effects on the phase structure of the pulse do occur, and could be seen in a many cycle regime.

[1] T. Brabec and F. Krausz, Phys. Rev. Lett. **78**, 3282 (1997), URL http://link.aps.org/abstract/PRL/v78/p3282.
[2] M. A. Porras, Phys. Rev. A **60**, 5069 (1999), URL http://link.aps.org/abstract/PRA/v60/p5069.
[3] Y. R. Shen, *Principles of nonlinear optics* (Wiley, 1984).
[4] A. V. Tarasishin, S. A. Magnitskii, and A. M. Zheltikov, Opt. Commun. **193**, 187 (2001), URL http://www.elsevier.com/gej-ng/10/34/18/96/23/47/abstract.html.
[5] T. Beddard, M. Ebrahimzadeh, D. T. Reid, and W. Sibbett, Opt. Lett. **25**, 1052 (2000), URL http://ol.osa.org/abstract.cfm?id=62075.
[6] A. Baltuska, Z. Wei, S. Pshenichnikov, and D. Wiersma, Opt. Lett. **22**, 102 (1997), URL http://ol.osa.org/abstract.cfm?id=35909.
[7] J. K. Ranka and A. L. Gaeta, Opt. Lett. **23**, 534 (1998), URL http://ol.osa.org/abstract.cfm?id=36664.
[8] S. Tzortzakis, L. Sudrie, M. Franco, B. Prade, A. Mysyrowicz, A. Couairon, and L. Berge, Phys. Rev. Lett. **87**, 213902 (2001), URL http://link.aps.org/abstract/PRL/v87/e213902.
[9] N. Akozbek, M. Scalora, C. M. Bowden, and S. L. Chin, Opt. Commun. **191**, 353 (2001), URL http://www.elsevier.com/gej-ng/10/34/18/94/25/47/abstract.html.
[10] A. L. Gaeta, Opt. Lett. **27**, 924 (2002), URL http://ol.osa.org/abstract.cfm?id=68951.
[11] P. Kinsler and G. H. C. New, Phys. Rev. A **67** (2003), URL http://link.aps.org/abstract/PRA/v67/e023813.
[12] S. M. Gallagher-Faeder and D. M. Jonas, Phys. Rev. A **62**, 033820 (2000), URL http://link.aps.org/abstract/PRA/v62/e033820.
[13] P. Kinsler, arXiv.org (2002), physics/0212014, URL http://arXiv.org/physics/0212014.
[14] D. H. Jundt, Opt. Lett. **22**, 1553 (1997), URL http://ol.osa.org/abstract.cfm?id=36381.